Nanoscale

PAPER

View Article Online
View Journal | View Issue

Cite this: *Nanoscale*, 2024, **16**, 6627

Copper single-site engineering in MOF-808 membranes for improved water treatment†

Isabel del Castillo-Velilla, [a] Ignacio Romero-Muñiz,[a] Carlo Marini,[b] Carmen Montoro *[a,c] and Ana Eva Platero-Prats *[a,d]

Received 16th November 2023,
Accepted 7th March 2024

DOI: 10.1039/d3nr05821b

rsc.li/nanoscale

MOF-808, a metal–organic framework containing Zr_6O_8 clusters, can serve as a secure anchoring point for stabilizing copper single-sites with redox activity, thus making it a promising candidate for catalytic applications. In this study, we target the incorporation of Cu-MOF-808 into a mixed-matrix membrane for the degradation of tyrosol, an emerging endocrine-disrupting compound commonly found in water sources, through Fenton reactions, developing innovative technologies for water treatment. We successfully demonstrate the effectiveness of this approach by preparing catalytic membranes with minimal metal leaching, which is one of the primary challenges in developing copper-based Fenton heterogeneous catalysts. Furthermore, we utilized advanced synchrotron characterization techniques, combining X-ray absorption spectroscopy and pair distribution function analysis of X-ray total scattering, to provide evidence of the atomic structure of the catalytic copper sites within the membranes. Additionally, we observed the presence of weak interactions between the MOF-808 and the organic polymer, potentially explaining their enhanced stability.

Introduction

The presence of endocrine-disrupting compounds (EDCs) in drinking water sources is of growing concern due to their potential to mimic hormones in our bodies and cause severe health problems.[1,2] Among them, alkyl phenol pollutants are a big group of natural constituents of petroleum oil and may be found in produced water discharged from offshore oil and gas installations. Their complex chemical nature makes their degradation in wastewater a significant challenge.[3] Various chemical methods have been employed to tackle the removal of organic water pollutants from wastewater, such as coagulation, hydrolysis, ion exchange, and chemical precipitation.[4] However, these technologies are often associated with high operating costs, toxic by-products, and limited degradation of EDCs.[5] To address these limitations, advanced oxidation processes stand out as efficient techniques due to their high oxidation efficacy and lack of secondary pollutants. One example are Fenton reactions, which have garnered attention for their versatility and effectiveness in removing organic pollutants from water.[6] However, the recyclability of Fenton-like technologies is often limited by active site leaching under common working conditions.[7]

In this context, crystalline porous materials such as Metal–Organic Frameworks (MOFs) present interesting properties towards the removal of emerging water pollutants.[8–11] Some of them are related to their large specific surface areas and pore volumes, associated with high sorption capacities; stabilization of active sites, where pollutants can be adsorbed and degraded; high stability in water (some of them); chemical tailorability; potential for large-scale synthesis and manufacturing as monoliths, pellets, membranes, or columns, for their implementation in decontamination devices.[12–15] Among the large family of MOFs, those based on Zr(IV)-oxo clusters are the most promising materials for practical applications since they exhibit rich structural types and high chemical stability, especially in water. The $Zr_6(\mu_3\text{-}O)_4(\mu_3\text{-}OH)_4$ (or Zr_6O_8, for clarity) octahedral cluster is the secondary building unit (SBU) found in many archetypical Zr–MOFs, such as UiO-66, NU-1000, and MOF-808.[16–18] Zr–MOFs based on Zr_6O_8 structural units have been shown to be active in the degradation of

[a]*Departamento de Química Inorgánica, Facultad de Ciencias, Universidad Autónoma de Madrid, 28049 Madrid, Spain. E-mail: carmen.montoro@uam.es, ana.platero@uam.es*
[b]*CELLS – ALBA Synchrotron Radiation Facility, Carrer de la Llum 2-26, 08090, Cerdanyola del Vallès, Barcelona, Catalonia, Spain*
[c]*Institute for Advanced Research in Chemical Sciences (IAdChem), Universidad Autónoma de Madrid, 28049 Madrid, Spain*
[d]*Condensed Matter Physics Center (IFIMAC), Universidad Autónoma de Madrid, 28049 Madrid, Spain*

† Electronic supplementary information (ESI) available. See DOI: https://doi.org/10.1039/d3nr05821b

toxic compounds, mainly due to the combined presence of strong Lewis acid Zr(IV) sites and the basic nature of the –OH/–O ligands within the Zr_6O_8 clusters.[19,20] Furthermore, the incorporation of a second metal cation within the Zr–MOF framework, as a local functional defect, can induce new properties and modify the Lewis acidity of zirconia clusters making them even more active.[21] Thus, post-synthetic modifications can be used as a method to incorporate metal sites in Zr–MOFs for improving their catalytic activity by stabilizing active sites in the porous structure.[22] In this regard, MOF-808 is a promising material that has attracted much attention in the last years, due to the occurrence of open-sites within the Zr_6O_8 cluster. MOF-808 is composed of $[Zr_6(\mu_3\text{-}O)_4(\mu_3\text{-}OH)_4(HCOO)_6]$ clusters as SBUs surrounded by 6 benzene-1,3,5-tricarboxylic acid (BTC) molecules as linkers (Fig. 1A). In particular, the low connectivity of 6 of the SBUs within MOF-808 (*i.e.* UiO-66 has a connectivity of 12) allows a wide variety of chemical modifications, both by insertion of organic ligands and metal sites, opening new opportunities for the development of porous materials with improved properties.[23–25]

All these advantages of MOFs have been widely demonstrated at the laboratory scale; however, some difficulties linked to the processing of MOF powders have hindered their industrial application in many cases. In the field of water treatment, the use of a target material as a powder may cause unwanted secondary pollution, therefore an additional filtration step is required. Thus, there is an emerging interest in developing strategies for improving the processability of MOFs for practical applications.[26] In this sense, membranes allow energy savings for an industrial scenario,[27] and the possibility to use MOFs as a catalyst in flow processes, by minimizing the mass transport limitation characteristic of powders.[28,29]

Among all the existing types of membranes based on porous materials, we have focused on mixed matrix membranes (MMMs) which combine organic polymers and inorganic fillers.[30] MOFs have been implemented as inorganic fillers for the preparation of functional MMMs for more than one decade already.[31] MOF-based MMM devices have been widely used in continuous flow systems, but most research about MOF-based membranes has focused on the use of these membranes for applications in gas separations,[32] liquid-phase separations,[33] or extractions.[34] In this scenario, the application of MOF-based MMM as catalytic technologies under continuous flow conditions has been scarce,[35] albeit the great potential of these porous functional systems.

In this work, we describe the development of functional porous MMM devices that utilize MOF-808 modified with copper singles-sites to efficiently degrade EDCs, such as tyrosol, through Fenton reactions. To gain insight into the local structure of the redox-active copper sites stabilized within the MMM, we employed advanced synchrotron characterization techniques, including pair distribution function (PDF) analyses of X-ray total scattering data and Cu K-edge X-ray absorption spectroscopy (XAS). Our results demonstrate that the stabilization of Cu-MOF-808 nanoparticles (NPs) into an organic polymeric matrix by hydrogen bonding interactions, leads to significantly reduced copper leaching and mass transfer limitations, resulting in superior performance under continuous flow compared to the powder. These findings highlight the potential of stabilized copper single-sites within MMMs for efficient and sustainable water treatment applications.

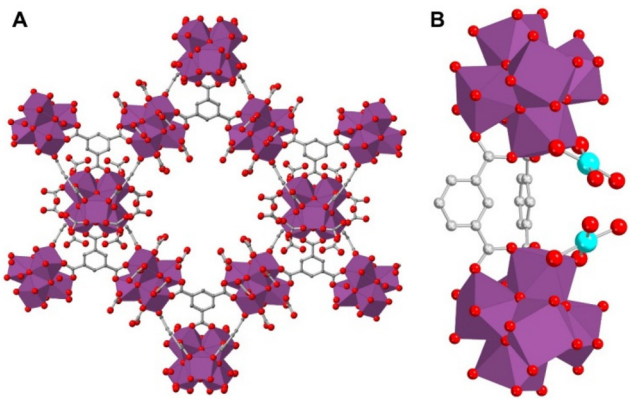

Fig. 1 (A) Representation of the MOF-808 structure. (B) Depiction of the copper single-sites grafted to the Zr_6O_8 clusters. Colour scheme: purple = Zr, grey = C, red = O, blue = Cu; hydrogen atoms have been omitted for clarity.

Results and discussion

Synthesis and characterization of the MOF nanoparticles

MOF-808 NPs were used for preparing MMMs to afford a homogenous dispersion of the MOF in the polymer matrix while avoiding aggregation and the formation of interfacial voids between the inorganic particles and the polymer.[36] Nano-sized MOF-808 was synthesized by microwave-assisted synthesis in *N,N*-Dimethylformamide (DMF) at 130 °C by exploring different reaction times (from 30 to 90 min). The as-prepared MOF-808 NPs were washed with DMF, distilled water, and methanol. The final washing with methanol affords the activation of the Zr_6O_8 cluster for further metalation with copper, by partially replacing the formate ligands by water and hydroxy groups.[37] The optimal results in terms of particle size, morphology, and crystallinity of MOF-808 NPs were obtained by using 45 min of reaction time (see S1, S3, S4 sections and Fig. S7.1 from ESI†). Subsequently, the MOF-808 NPs were metalated with copper by immersion in a solution of methanol containing copper(II) acetate, at 60 °C overnight. The resulting Cu-MOF-808 NPs were activated through several washings with methanol, distilled water, and ethanol where they were finally suspended to avoid aggregation. ICP analyses on the sample indicated a molar ratio Cu to Zr_6O_8 of *ca.* 3.1.

Powder X-ray diffraction (PXRD) data collected on the Cu-MOF-808 NPs showed the unique presence of the Bragg peaks corresponding to the MOF-808 phase, together with the retaining of long-range order within the structure (Fig. 2A). Fourier-transform infrared spectroscopy (FTIR) indicated the occur-

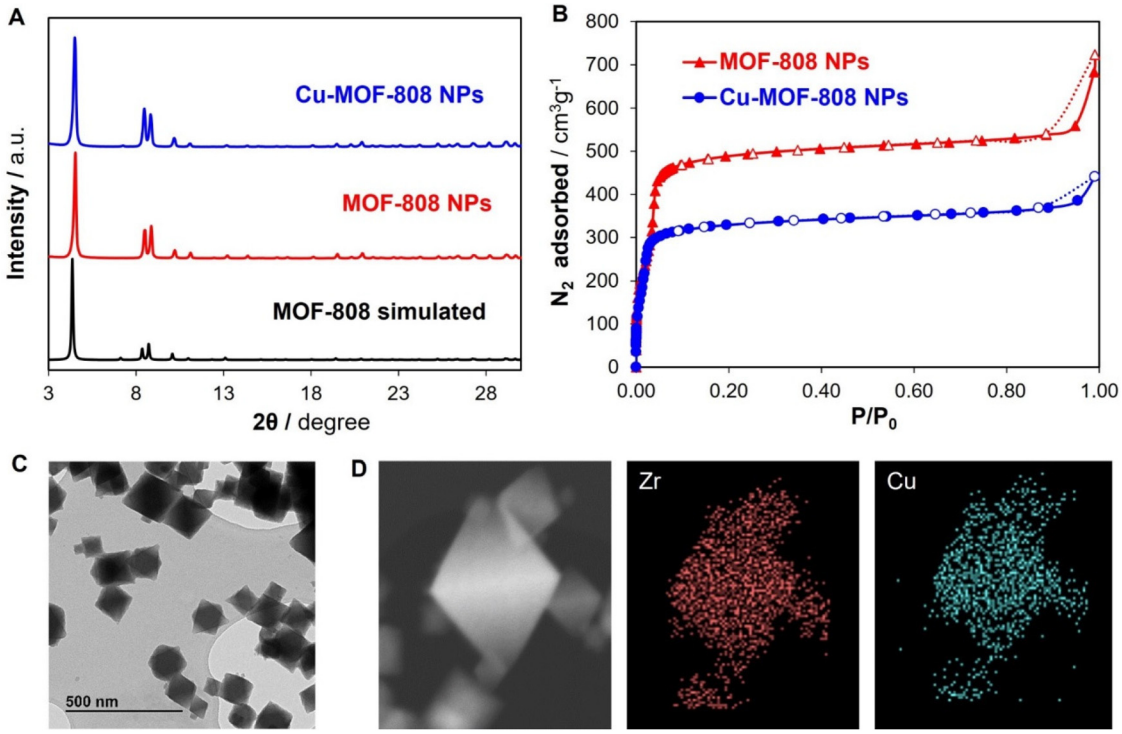

Fig. 2 (A) PXRD patterns of the synthesized materials and simulated for MOF-808. (B) N_2 adsorption isotherms at 77 K for MOF-808 and Cu–MOF-808 NPs. Filled and empty symbols correspond to adsorption and desorption processes, respectively. (C) TEM image of Cu–MOF-808 NPs. (D) Mapping of Zr and Cu for Cu–MOF-808 NPs.

rence of characteristic vibrational bands of the MOF-808 framework in the metalated material (see S8 section from ESI†).[38] Proton nuclear magnetic resonance (^{1}H-NMR) experiments on a digested sample of Cu–MOF-808 (see S2 section from ESI†) enabled us to quantify the chemistry of the organic component of the material, suggesting a chemical formula of $[Zr_6Cu_{3.1}O_8H_4(C_9H_3O_6)_2(OH)_{9.8}(H_2O)_{3.6}(C_2H_3O_2)_{2.4}]$. Thermal gravimetric analyses (TGA) showed thermal stability for Cu-MOF-808 NPs up to *ca.* 230 °C, similar to the pristine material (see S9 section from ESI†).

Nitrogen adsorption isotherms collected on the MOF-808 NPs before and after the incorporation of copper (Fig. 2B) revealed expected changes in the porosity of the material upon metalation. Particularly, the surface area for MOF-808 NPs is significantly larger than that of bulk MOF-808 (1712 $m^2\ g^{-1}$ reported for bulk MOF-808[38] compared to 2035 $m^2\ g^{-1}$ for MOF-808 NPs) and that of Cu-MOF-808 NPs (1370 $m^2\ g^{-1}$). This decrease in adsorption capacity is related to the incorporation of copper single sites along the edges of the tetrahedral cavities in MOF-808 (Fig. 1B), as previously seen for the bulk material.[39] Regarding the NLDFT pore size distribution calculation, while the Cu-loaded MOF NPs seem to maintain the micropore window (*ca.* 12 Å and *ca.*18 Å), the micropore taken as the pore width under 22 Å to the total pore volume rapidly decreases with the metal loading (see S10 section from ESI†).

The morphology of the synthesized Cu-MOF-808 NPs was studied by field emission scanning microscopy and transmission electron microscopy with energy dispersive X-ray spectroscopy (FE-SEM and TEM-EDS), showing a nanoparticle size of around 115 nm for Cu-MOF-808 (see S3 and 4 sections from ESI†). TEM-EDS with the complementary mapping analyses performed on the sample (Fig. 2C and D) showed the homogeneous incorporation of copper within the material. Dynamic light scattering (DLS) performed on Cu–MOF-808 NPs indicated an average hydrodynamic size of around 300 nm (see S6 section from ESI†). DLS measurements also demonstrated the excellent stability of the colloidal suspensions of the MOF NPs for 1 week.

Synthesis and characterization of the membranes

The remarkable colloidal stability of the Cu-MOF-808 NPs suspensions in different organic solvents allowed us to prepare crack-free and uniform MMMs by applying the casting method. For that, a solution of polyvinylidene fluoride (PVDF) in DMF at 5 wt% was added to a suspension of MOF NPs in DMF at 15 wt%. After solvent evaporation, MMMs with good mechanical stability and flexibility were obtained (see S1 section from ESI† for detailed information).

PXRD data of the Cu-MOF-808 MMMs is dominated by the Bragg peaks corresponding to the MOF-808 phase, although the appearance of some broad signals corresponding to the disordered PVDF matrix is also observed (Fig. 3A). FTIR spectra further showed the successful incorporation of the MOF NPs within the PVDF matrix. By the assignment of

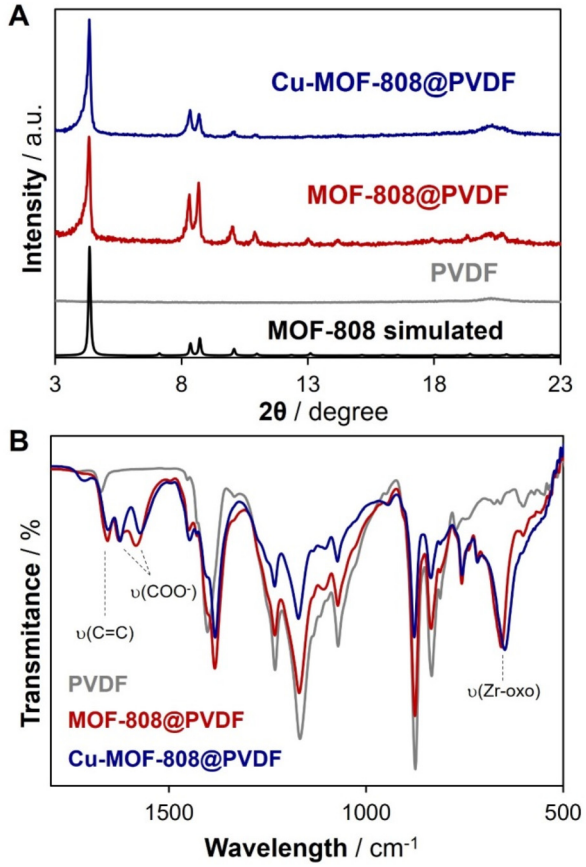

Fig. 3 (A) PXRD data of the synthesized membranes and the simulated for MOF-808.[37] (B) FTIR spectra of both MMMs compared to the PVDF membrane.

characteristic bands at 1651 cm^{-1} linked to the benzene ring from the organic ligands; at 1624 and 1581 cm^{-1} linked to the vibration of the carboxylate groups; and at 650 cm^{-1} linked to collective vibrations of the Zr_6O_8 cluster involving multiple Zr–O bonds (Fig. 3B).

To assess the morphology and the homogeneity, the membranes were characterized by SEM and EDS mapping (Fig. 4, and S5 section from ESI†). The results showed the homogeneous incorporation of the MOF NPs within the PVDF matrix in both cases. The SEM cross-section images revealed membrane thicknesses of around 140 μm for the Cu-MOF-808@PVDF membranes.

Advanced synchrotron characterization was performed by combining XAS and PDF analyses to assess the atomic structure of the catalytically active copper sites within the Cu-MOF-808@PVDF membrane (see S11 and S12 sections from ESI†). XAS experiments were carried out to elucidate both the geometry and the oxidation state of copper within the membrane. Cu K-edge X-ray absorption near-edge structure (XANES) data of Cu-MOF-808@PVDF obtained at 20 K showed two main features (Fig. 5A). The pre-edge peak was observed at 8979 eV, which is consistent with the presence of Cu(II) in a twisted-square-planar geometry.[40] An additional feature is observed at 8986 eV which corresponds with the 1s → {4p + shakedown} transition.[41] The Cu K-edge extended X-ray absorption fine structure (EXAFS) data indicated a main peak centred at 1.6 Å (without phase correction) that corresponds to the Cu(II)–O bonds, together with the absence of contributions beyond *ca.* 2.2 Å characteristic of copper aggregates (Fig. 5B). This evidences the presence of Cu(II) single-sites stabilized within the composite membrane.

PDF analyses of X-ray total scattering data were carried out to assess the local structure of the membrane components (that is, PVDF and Cu-MOF-808) as well as the presence of

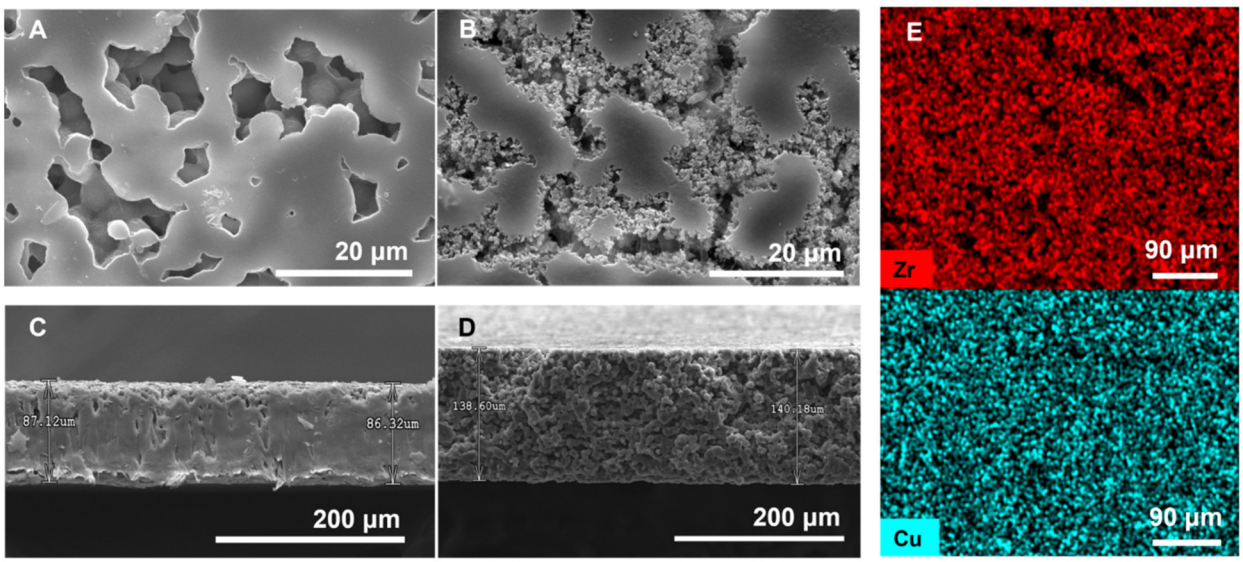

Fig. 4 SEM images of the top view of (A) the surface of PVDF and (B) Cu-MOF-808@PVDF membranes. SEM cross-section image of (C) PVDF and (D) Cu-MOF-808@PVDF membranes. (E) SEM-EDS elemental mapping of Zr (red) and Cu (blue) for Cu–MOF-808@PVDF MMM.

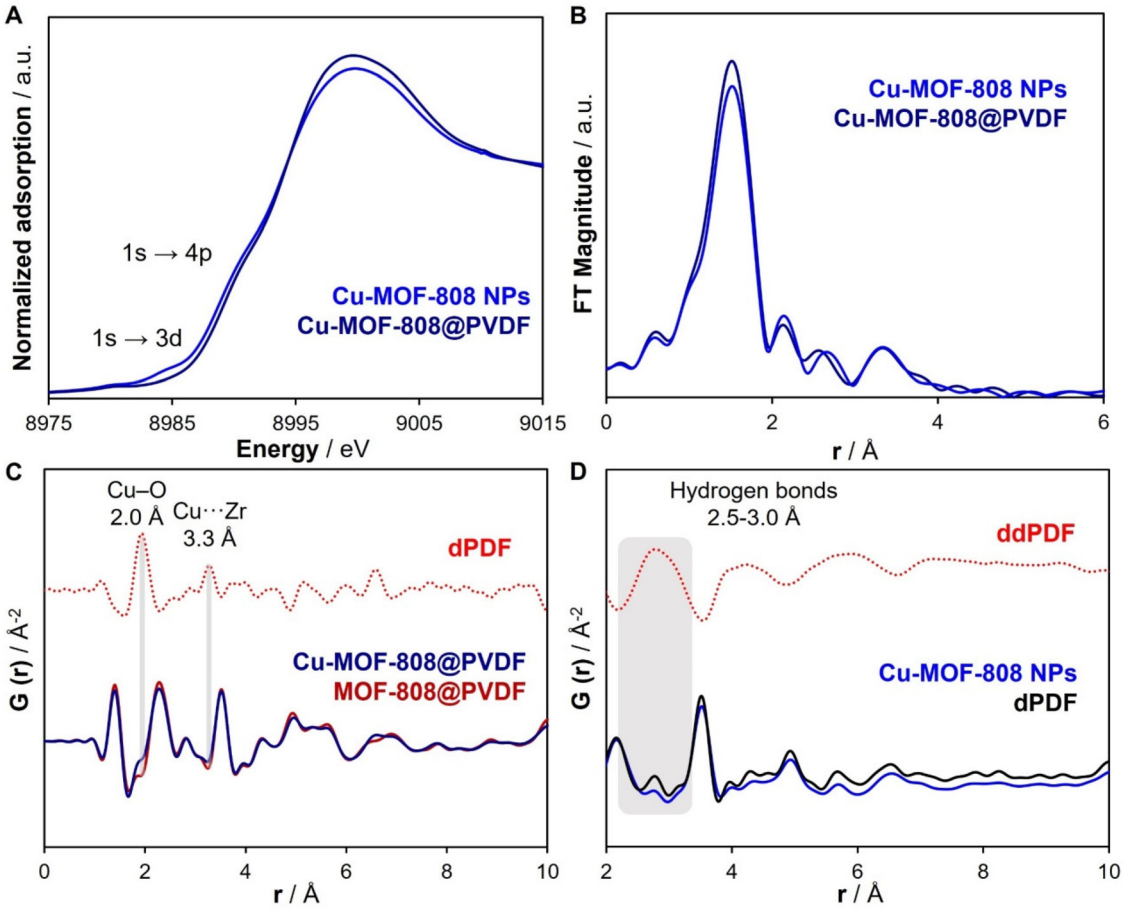

Fig. 5 (A and B) XAS analysis. (A) Cu K-edge XANES for Cu-MOF-808 NPs and Cu-MOF-808@PVDF membrane collected at 20 K. (B) EXAFS data for Cu-MOF-808 NPs and Cu-MOF-808@PVDF membrane collected at 20 K. (C and D) PDF analysis (C) dPDF data comparing the PDF pattern of the MOF-808@PVDF and Cu-MOF-808@PVDF MMMs. (D) ddPDF data (up) obtained after subtracting the total PDF data of Cu-MOF-808 NPs from the dPDF obtained from comparing Cu-MOF-808@PVDF with PVDF (down).

specific molecular interactions at the interface formed between the MOF and the polymer. Due to the complex composite structure of the membranes, a variety of differential analyses of the PDF data (dPDF) were performed to answer different questions regarding the structure of the composite at the local scale. To first assess the retaining of the MOF local structure within the composite, the PDF signal of the polymeric matrix PVDF was subtracted from the total PDF profile of Cu-MOF-808@PVDF. Thus, the contributions associated with the Cu–MOF-808 phase into the MMM were identified. This dPDF signal shows a broad peak centred at *ca.* 2.2 Å linked to Zr–O bonds and two sharp signals centred at *ca.* 3.5 and 5.0 Å corresponding to Cu···Zr and Zr···Zr distances characteristic of the Zr_6O_8 clusters within the MOF-808 structure (Fig. 5C). A similar PDF fingerprint is seen for bulk Cu-MOF-808, thereby corroborating the retaining of the local structure of the MOF within the composite membranes (see Fig. S12.1 from ESI†).

Further PDF differential analyses were then performed to elucidate both the atomic structure and specific location of the copper single sites within the membranes. Thus, the PDF signal of a MOF-808-loaded membrane was subtracted from that of Cu-MOF-808@PVDF. This dPDF signal highlighted the fingerprint of the copper species stabilized within the MOF-808 structure, with characteristic features centred at *ca.* 2.0 and 3.3 Å linked to Cu–O and Cu···Zr distances, respectively (Fig. 5D). The occurrence of these two PDF peaks demonstrates the presence of copper-oxo singles-sites attached to the Zr_6O_8 nodes along the tetrahedral cavities in MOF-808.[39] This evidence corroborates the stabilization of heterobimetallic Zr(IV)–Cu(II)–oxo nanostructures within the MOF-808 porous structure within the composite membranes.

With the aim of further understanding the potential occurrence of specific molecular interactions between the MOF and the PVDF phases at the interface of the composite, subsequent differential PDF analyses were carried out. Thus, the PDF signals of both Cu-MOF-808 and PVDF samples were subtracted from the MMM. In the case of a lack of any interaction between the MOF and the polymeric phase (*i.e.* physical mixture), this dPDF would result in a flat signal. In other words, the structure of the MMM could be simply described as a summary of structures. Interestingly, by applying dPDF ana-

lyses a group of weak signals were identified in the range of *ca.* 2.5–3.0 Å, which could be assigned to O···F distances, due to the presence of hydrogen bonding between the MOF and the polymeric matrix (Fig. 5D). This result demonstrated a synergistic stabilization of the Cu-MOF-808 within the PVDF polymer, by the formation of weak and strong molecular interactions.

Catalytic degradation of tyrosol

The catalytic activity of the prepared Cu-MOF-808@PVDF membrane was evaluated for the degradation of tyrosol (TyrOH) in water, a phenolic olive oil mill wastewater, through oxidation processes. Fenton-like reactions with copper heterogeneous catalysts have been extensively studied and, in most cases, the major drawback is the copper leaching during catalysis.[42–44] This catalyst deactivation through leaching can be explained by the solubility of copper(II) aqua complexes in water at acid pH values. During the catalytic cycle (see S13 section from ESI†), protons are released, thereby lowering the pH and causing catalyst deactivation. This pH variation is therefore difficult to prevent. In this work, we have been able to minimize copper leaching by stabilizing the catalyst NPs into a robust MMM.

Degradation experiments through Fenton-like reactions were carried out for solutions of 500 ppm of TyrOH in water at pH = 6 (natural of the solution). First, the catalytic performance of the Cu-MOF-808 NPs, as powder, was evaluated under batch conditions. Thus, a sample of Cu-MOF-808 NPs (0.009 mmol Cu) was added to a static solution of TyrOH (0.018 mmol in water) and hydrogen peroxide (0.24 mmol, 30% in water) at 60 °C. After 180 min, the reaction was cooled down and the yellowish supernatant liquid was then analyzed by UV-Visible spectroscopy, indicating a degradation of TyrOH of 90%.

Remarkably, the catalytic activity of Cu-MOF-808 NPs significantly decreased after four cycles from 90% to 30% degradation of TyrOH, thereby suggesting a fast deactivation process. The materials after catalysis were characterized by PXRD, FTIR, ICP, EXAFS, and PDF (see S7, S8, S11, S12, and S13 sections from ESI†). The ICP results showed that the deactivation of the Cu-MOF-808 NPs was related to significant copper leaching, with a loss of 70% of Cu sites after each cycle. Hot filtration experiments and ICP analyses demonstrated that the performance of Cu–MOF-808 NPs towards the degradation of TyrOH is mainly in the homogeneous phase, due to the accused loss of copper sites during catalysis.

Interestingly, the incorporation of Cu-MOF-808 NPs into a polymer matrix resulted in an improved catalytic performance in the heterogeneous phase, by significantly diminishing the copper leaching even after 4 cycles. Thus, the experiments showed that the Cu-MOF-808@PVDF membrane degrades 90% of TyrOH after the first cycle. Furthermore, the copper leaching when using the membrane is half of that observed in the case of the Cu-MOF-808 powder (Fig. 6A), suggesting that the PVDF matrix favours the stabilization of copper, and the catalysis occurs in the heterogeneous phase.

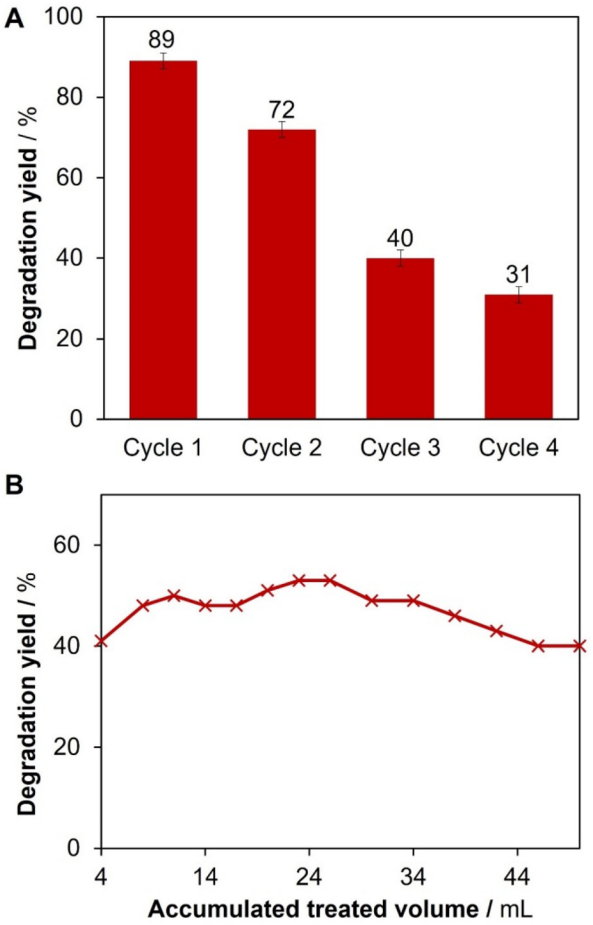

Fig. 6 (A) Cycles of TyrOH degradation by using Cu-MOF-808@PVDF under batch conditions. (B) Evolution of the TyrOH degradation by using Cu-MOF-808@PVDF under continuous flow.

The excellent catalytic results described for the Cu-MOF-808@PVDF membrane encouraged us to evaluate its performance under real operating conditions for the removal of ECDs in water. For this purpose, a custom-made catalytic membrane reactor was used to operate under flow conditions where Cu-MOF-808@PVDF was placed, then a feed solution of TyrOH (0.018 mmol in water) with hydrogen peroxide (0.24 mmol, 30% in water) was pumped through at a flux of 0.15 mL min^{-1} for 8 h (see S13 section from ESI† for detailed information). The reaction progress was monitored by UV–Visible spectroscopy. Remarkably, a continuous conversion of TyrOH of *ca.* 50% was constantly observed for over 5 h, which is equivalent to 50 mL of treated solution, degrading in total five times more pollutant than under batch conditions (Fig. 6B). The chemical composition of the membranes after their use was determined by ICP, corroborating a minimized copper leaching of 20% after 5 h compared to the 70% seen for the powder after only one cycle.

To assess the synergistic effect between the copper single-sites and the Zr_6O_8 clusters within the heterobimetallic Cu(II) Zr(IV)-oxo units in Cu-MOF-808 (Fig. 1B), a series of compara-

tive analyses were performed. With this purpose, the well-known Cu–BTC or HKUST-1 MOF,[45] which is composed of paddlewheel copper clusters as SBUs, was prepared in the form of NPs and tested as a Fenton catalyst for the degradation of TyrOH under batch conditions. Contrary to Cu-MOF-808, the Cu–BTC MOF completely degrades during the reaction upon low stability in water and copper leaching. Furthermore, a MMM containing Cu–BTC NPs was prepared and tested under flow conditions. The results obtained showed a higher copper leaching for Cu-BTC@PVDF compared to Cu-MOF-808@PVDF (32% of copper loss per hour) (see S13 section from ESI†), thereby highlighting the importance of stabilizing copper sites into Zr–MOFs for their use as Fenton catalysts.

The Cu-MOF-808@PVDF membranes after catalysis were also characterized by XRD and FTIR, demonstrating that the MOF crystallinity and the integrity of the membrane components are retained (see S7 and S8 sections from ESI†). EXAFS analyses of Cu K-edge XAS data further corroborated the retaining of the copper(II) single-sites within MOF-808, with main contributions at 1.6 Å characteristic of Cu–O bonds and the absence of a signal at 2.4 A attributed to Cu···Cu distance in CuO (Fig. 7A). With the aim of demonstrating the stability of the copper sites within the membranes, PDF analyses were performed on the Cu-MOF-808@PVDF membrane after 8 h of reaction (Fig. 7B). The dPDF profiles of the Cu single sites were obtained by subtracting the MOF-808@PVDF evidencing the absence of major changes at the local scale and the data was also compared with the simulated pattern of CuO, thereby demonstrating the lack of evolution to other copper species which may also catalyse Fenton reactions.

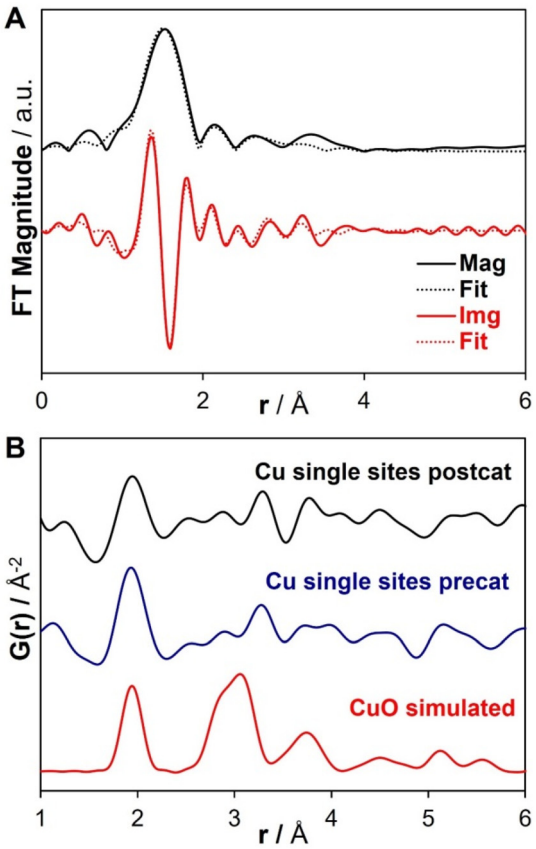

Fig. 7 (A) EXAFS k^2-weighted Cu K-edge Mag[$\chi(R)$] and Img[$\chi(R)$] (solid lines) spectra with their respective fits (dash lines) of Cu–MOF-808@PVDF after catalysis. (B) PDF characterization of the Cu singles sites in the MMMs before and after catalysis compared with CuO data.

Conclusions

In conclusion, we have successfully stabilized redox-active Cu-MOF-808 NPs into a mixed-matrix membrane for the degradation of TyrOH in water *via* Fenton-like reactions. Our findings reveal that the composite nature of the MMM enhanced the material's applicability under real operating conditions, reducing copper leaching by over 50% compared to the MOF powder. Synchrotron XAFS and PDF characterization demonstrated the atomic structure of the copper sites within the membranes, as well as the presence of weak interactions between the MOF phase and the PVDF polymer that may explain the enhanced stability of the catalyst. Further investigations are currently underway to elucidate the structural features of the MOF–PVDF interface, which can aid in the development of advanced membranes with improved catalytic properties for environmental remediation applications.

Author contributions

The manuscript was written through the contributions of all authors. All authors have given approval to the final version of the manuscript.

Conflicts of interest

There are no conflicts to declare.

Acknowledgements

This work was supported by PID2021-123839OB-I00 funded by MCIN/AEI/10.13039/501100011033 and FEDER, UE; EUR2020-112294 and CNS2022-135261 funded by MICIU/AEI/10.13039/501100011033 and by "European Union NextGenerationEU/PRTR"; and RYC2018-024328-I by funded by MICIU/AEI/10.13039/501100011033 and by "ESF Investing in your future". A. E. P.-P. acknowledges the financial support from the Spanish Ministry of Science and Innovation, through the "María de Maeztu" Programme for Units of Excellence in R&D (CEX2018-000805-M). C. M. acknowledges the financial support of the Madrid Government under the Multiannual Agreement with Universidad Autónoma de Madrid in the context of the V PRICIT (SI1/PJI/2019–00505). I. C.-V. acknowledges FPI-UAM 2021 fellowship UAM. The authors would like

to thank Diamond Light Source for beamtime (proposal CY30311), and Dr Philip Chater and I15-1 staff for his assistance with PDF data collection. We acknowledge DESY (Hamburg, Germany), a member of the Helmholtz Association HGF, for the provision of experimental facilities. Part of this research was carried out at PETRA III and we would like to thank Dr S. J. Méndez for her assistance in using the P02.1 beamline for collecting preliminary PDF data relevant to this work. Beamtime was allocated for proposal I-20211230 EC. XAS experiments were performed at the BL22 beamline (proposal 2021024939) at ALBA Synchrotron with the collaboration of ALBA staff.

References

1 E. Diamanti-Kandarakis, J. P. Bourguignon, L. C. Giudice, R. Hauser, G. S. Prins, A. M. Soto, R. T. Zoeller and A. C. Gore, *Endocr. Rev.*, 2009, **30**, 293–342.
2 S. Y. Wee and A. Z. Aris, *npj Clean Water*, 2019, **2**, 1–14.
3 J. Singh, V. Saharan, S. Kumar, P. Gulati and R. K. Kapoor, *Crit. Rev. Biotechnol.*, 2017, **38**, 883–901.
4 I. A. Saleh, N. Zouari and M. A. Al-Ghouti, *Environ. Technol. Innovation*, 2020, **19**, 101026–101048.
5 M. Ahmed, M. O. Mavukkandy, A. Giwa, M. Elektorowicz, E. Katsou, O. Khelifi, V. Naddeo and S. W. Hasan, *npj Clean Water*, 2022, **5**, 1–25.
6 J. Wang and R. Zhuan, *Sci. Total Environ.*, 2020, **701**, 135023–135038.
7 S. Navalon, M. Alvaro and H. Garcia, *Appl. Catal., B*, 2010, **99**, 1–26.
8 S. Rojas and P. Horcajada, *Chem. Rev.*, 2020, **120**, 8378–8415.
9 M. Mon, R. Bruno, J. Ferrando-Soria, D. Armentano and E. Pardo, *J. Mater. Chem. A*, 2018, **6**, 4912–4947.
10 L. Joseph, B. M. Jun, M. Jang, C. M. Park, J. C. Muñoz-Senmache, A. J. Hernández-Maldonado, A. Heyden, M. Yu and Y. Yoon, *Chem. Eng. J.*, 2019, **369**, 928–946.
11 E. Jin, S. Lee, E. Kang, Y. Kim and W. Choe, *Coord. Chem. Rev.*, 2020, **425**, 213526–213555.
12 X. Liu, X. Wang and F. Kapteijn, *Chem. Rev.*, 2020, **120**, 8303–8377.
13 M. Kalaj, K. C. Bentz, S. Ayala, J. M. Palomba, K. S. Barcus, Y. Katayama and S. M. Cohen, *Chem. Rev.*, 2020, **120**, 8267–8302.
14 S. Yu, H. Pang, S. Huang, H. Tang, S. Wang, M. Qiu, Z. Chen, H. Yang, G. Song, D. Fu, B. Hu and X. Wang, *Sci. Total Environ.*, 2021, **800**, 149662–149684.
15 J.-Y. Lee, C. Y. Tang and F. Huo, *Sci. Rep.*, 2014, **4**, 3740–3745.
16 J. H. Cavka, S. Jakobsen, U. Olsbye, N. Guillou, C. Lamberti, S. Bordiga and K. P. Lillerud, *J. Am. Chem. Soc.*, 2008, **130**, 13850–13851.
17 J. E. Mondloch, W. Bury, D. Fairen-Jimenez, S. Kwon, E. J. Demarco, M. H. Weston, A. A. Sarjeant, S. T. Nguyen, P. C. Stair, R. Q. Snurr, O. K. Farha and J. T. Hupp, *J. Am. Chem. Soc.*, 2013, **135**, 10294–10297.
18 J. Jiang, F. G. Gándara, Y.-B. Zhang, K. Na, O. M. Yaghi and W. G. Klemperer, *J. Am. Chem. Soc.*, 2014, **136**, 12844–12847.
19 Y. Bai, Y. Dou, L.-H. Xie, W. Rutledge, J.-R. Li and H.-C. Zhou, *Chem. Soc. Rev.*, 2016, **45**, 2327–2367.
20 F. Bi, Z. Zhao, Y. Yang, W. Gao, N. Liu, Y. Huang and X. Zhang, *Environ. Sci. Technol.*, 2022, **56**, 17321–17330.
21 M. Rimoldi, A. J. Howarth, M. R. Destefano, L. Lin, S. Goswami, P. Li, J. T. Hupp and O. K. Farha, *ACS Catal.*, 2017, **7**, 997–1014.
22 Z. Fang, B. Bueken, D. E. De Vos and R. A. Fischer, *Angew. Chem., Int. Ed.*, 2015, **54**, 7234–7254.
23 J. Zhang, S. B. Peh, J. Wang, Y. Du, S. Xi, J. Dong, A. Karmakar, Y. Ying, Y. Wang and D. Zhao, *Chem. Commun.*, 2019, **55**, 4727–4730.
24 C. Castillo-Blas, I. Romero-Muñiz, A. Mavrandonakis, L. Simonelli and A. E. Platero-Prats, *Chem. Commun.*, 2020, **56**, 15615–15618.
25 J. Baek, B. Rungtaweevoranit, X. Pei, M. Park, S. C. Fakra, Y. S. Liu, R. Matheu, S. A. Alshmimri, S. Alshehri, C. A. Trickett, G. A. Somorjai and O. M. Yaghi, *J. Am. Chem. Soc.*, 2018, **140**, 18208–18216.
26 P. Cheng, C. Wang, Y. V. Kaneti, M. Eguchi, J. Lin, Y. Yamauchi and J. Na, *Langmuir*, 2020, **36**, 4231–4249.
27 Q. Chen, L. Hong, S. K. Jiang, C. X. Zhang, S. Wang, W. X. Li, S. P. Sun and M. L. Liu, *J. Membr. Sci.*, 2023, **675**, 121520–121528.
28 C. Huang, Z. Guo, X. Zheng, X. Chen, Z. Xue, S. Zhang, X. Li, B. Guan, X. Li, G. Hu and T. Wang, *J. Am. Chem. Soc.*, 2020, **142**, 9408–9414.
29 G. Dong, H. Li and V. Chen, *J. Mater. Chem. A*, 2013, **1**, 4610–4630.
30 M. L. Liu, C. X. Zhang, M. J. Tang, S. P. Sun, W. Xing and Y. M. Lee, *Prog. Mater. Sci.*, 2023, **139**, 101162–101190.
31 R. Thür, N. Van Velthoven, V. Lemmens, M. Bastin, S. Smolders, D. De Vos and I. F. J. Vankelecom, *ACS Appl. Mater. Interfaces*, 2019, **11**, 44792–44801.
32 S. Castarlenas, C. Téllez and J. Coronas, *J. Membr. Sci.*, 2017, **526**, 205–211.
33 X. Li, Y. Liu, J. Wang, J. Gascon, J. Li and B. van der Bruggen, *Chem. Soc. Rev.*, 2017, **46**, 7124–7144.
34 G. Wu, J. Ma, S. Wang, H. Chai, L. Guo, J. Li, A. Ostovan, Y. Guan and L. Chen, *J. Hazard. Mater.*, 2020, **394**, 122556–122567.
35 J. Hou, Y. Luan, X. Huang, H. Gao, M. Yang and Y. Lu, *New J. Chem.*, 2017, **41**, 9123–9129.
36 B. Ghalei, K. Sakurai, Y. Kinoshita, K. Wakimoto, A. P. Isfahani, Q. Song, K. Doitomi, S. Furukawa, H. Hirao, H. Kusuda, S. Kitagawa and E. Sivaniah, *Nat. Energy*, 2017, **2**, 1–9.
37 H. Furukawa, F. Gándara, Y. B. Zhang, J. Jiang, W. L. Queen, M. R. Hudson and O. M. Yaghi, *J. Am. Chem. Soc.*, 2014, **136**, 4369–4381.

38 I. Romero-Muñiz, C. Romero-Muñiz, I. Del Castillo-Velilla, C. Marini, S. Calero, F. Zamora and A. E. Platero-Prats, *ACS Appl. Mater. Interfaces*, 2022, **14**, 27040–27047.
39 I. del Castillo-Velilla, A. Sousaraei, I. Romero-Muñiz, C. Castillo-Blas, A. S. J. Méndez, F. E. Oropeza, V. A. de la Peña O'Shea, J. Cabanillas-González, A. Mavrandonakis and A. E. Platero-Prats, *Nat. Commun.*, 2023, **14**, 2506–2516.
40 M. L. Baker, M. W. Mara, J. J. Yan, K. O. Hodgson, B. Hedman and E. I. Solomon, *Coord. Chem. Rev.*, 2017, **345**, 182–208.
41 G. R. Shulman, Y. Yafet, P. Eisenberger and W. E. Blumberg, *Proc. Natl. Acad. Sci. U. S. A.*, 1976, **73**, 1384–1388.
42 Y. Sheng, Y. Sun, J. Xu, J. Zhang and Y. F. Han, *AIChE J.*, 2018, **64**, 538–549.
43 M. Fang, R. Zheng, Y. Wu, D. Yue, X. Qian, Y. Zhao and Z. Bian, *Environ. Sci.: Nano*, 2019, **6**, 105–114.
44 J. Tang and J. Wang, *Chem. Eng. J.*, 2019, **375**, 122007–122018.
45 S. S. Y. Chui, S. M. F. Lo, J. P. H. Charmant, A. G. Orpen and I. D. Williams, *Science*, 1999, **283**, 1148–1150.